Simultaneous Imaging and Diffraction in the dynamic Diamond Anvil Cell

R. J. Husband[1,a)], J. Hagemann[2], E. F. O'Bannon[3], H.-P. Liermann[1], K. Glazyrin[1], D. T. Sneed[3], M. J. Lipp[3], A. Schropp[2], W. J. Evans[3] and Zs. Jenei[3]

[1]Deutsches Elektronen-Synchrotron DESY, Notkestr. 85, 22607 Hamburg, Germany

[2] Center for X-ray and Nano Science CXNS, Deutsches Elektronen-Synchrotron DESY, Notkestr. 85, 22607 Hamburg, Germany

[3]Physics Division, Physical & Life Sciences Directorate, Lawrence Livermore National Laboratory, Livermore, CA 94550, USA

[a)]Author to which correspondence should be addressed: rachel.husband@desy.de

Abstract

The ability to visualize a sample undergoing a pressure-induced phase transition allows for the determination of kinetic parameters such as the nucleation and growth rates of the high-pressure phase. For samples that are opaque to visible light (such as metallic systems), it is necessary to rely on X-ray imaging methods for sample visualization. Here, we present an experimental platform developed at beamline P02.2 at the PETRA III synchrotron radiation source, which is capable of performing simultaneous X-ray imaging and diffraction of samples which are dynamically-compressed in piezo-driven diamond anvil cells (DACs). This set-up utilizes a partially-coherent monochromatic X-ray beam to perform lens-less phase contrast imaging (PCI), which can be carried out using either a parallel or focused-beam configuration. The capabilities of this platform are illustrated by experiments on dynamically-compressed Ga and Ar. Melting and solidification were identified based on the observation of solid/liquid phase boundaries in the X-ray images and corresponding changes in the X-ray diffraction patterns collected during the transition, with significant edge enhancement observed in the X-ray images collected using the focused-beam. These results highlight the suitability of this technique for a variety of purposes including melt curve determination.

I. Introduction

X-ray diffraction and spectroscopic studies of samples confined at high pressures in DACs are commonly-performed at synchrotron radiation sources at specialized beamlines[1–3]; consequently, the structural and electronic behavior of many materials have been well characterised up to 100 GPa (1 Mbar). Previous DAC studies have revealed that many materials exhibit complex behaviour at high pressures, where compression can drive transformations to low symmetry structures (reference [4] and references therein), induce dramatic changes in electronic properties[5], or produce anomalous melting behaviour[6,7]. However, although X-ray diffraction provides crystallographic information corresponding to nm length scales (averaged over the area illuminated by the X-ray beam), studies investigating the sample behaviour on microscopic (µm) length scales (i.e. the dimension of the sample chamber) are scarce.

Time-resolved imaging of samples in the DAC can provide insight into the kinetics of structural phase transitions. When crystallite sizes (or melt regions) are relatively large with well-defined phase boundaries, it is possible to visualize the growth of the new phase. This allows for the direct determination of kinetic parameters such as growth rates, identification of nucleation sites within the sample chamber (e.g. at the gasket edge or at an internal pressure standard), as well as monitoring of crystal morphology. Understanding the nucleation and growth process is important for industrial processes, as control of the crystallization process is used to tune properties such as grain size which, in turn, influences physical properties such as hardness (e.g. Hall-Petch strengthening) and material toughness[8].

Investigation of phase transition kinetics requires control of at least one independent thermodynamic variable to drive the sample through the transition. The study of pressure-driven transitions offers several advantages over those which are temperature driven. For example, pressure can induce significantly larger changes in interatomic distances; consequently, high-pressure structural polymorphs tend to be more numerous than those stabilized by temperature alone. In addition, while heating and cooling rates are inherently limited by the thermal conductivity of the sample and heating assembly, control of the compression rate is limited primarily by the rate at which the external force is applied to the DAC. Precise control of the sample pressure can be achieved through the use of piezo-driven dynamic DACs (dDACs) in which the pressure-time profile can be tailored by the application of a user-defined voltage waveform to a piezo actuator driver[9,10]. The dDAC is also capable of generating extremely fast compression rates (up to 160 TPa/s[10]), which allows for the study of rate-dependent behaviour[11–16].

Initial dDAC studies relied on optical imaging and spectroscopy measurements as diagnostic probes; consequently, they mostly focused on transparent molecular systems such as H_2O[11–13,16] and H_2[14]. In addition to revealing several compression-rate dependent transition pathways in H_2O[11,13], previous studies showed that the crystal morphology and growth rate of ice VI is influenced by compression rate[12,16], displaying a cross-over from 3D to 2D growth at strain rates $>7\text{x}10^{-2}$ s^{-1} [16]. More recently, the development of high speed (kHz) hybrid pixel photon counting detectors for hard X-rays enabled dDAC studies to utilize time-resolved X-ray diffraction for direct structural determination[10,15,17,18]. Recent work reported an over-pressurization of the Bi-III/Bi-V phase boundary by as much as 2.5 GPa at compression rates below 1000 GPa/s, suggesting that dDAC compression timescales are suitable for the study of transition kinetics in metallic systems[15]. Diffraction studies are now possible even for low-Z materials, but have focused primarily on equation of state measurements rather than rate-dependent behavior[17]. However, to-date, simultaneous imaging and diffraction experiments have not been reported for dDAC compressed samples.

In order to extend dDAC imaging studies to samples which are opaque to visible light (e.g. metallic systems), it is necessary to utilize X-ray imaging techniques. X-ray radiography, in which the transmitted intensity is related to the X-ray absorption coefficient and sample thickness via the Beer Lambert law, has long been used in conjunction with the large volume press to measure a range of physical properties such as density[19], melting[20], immiscibility behavior[21,22], strain[23], and viscosity [24–30], and to determine the equation of state of amorphous materials in the DAC[31]. However, one drawback of absorption-based imaging is that it produces poor contrast for low-Z materials as the absorption coefficient is ~Z^4 [32]. This method is therefore generally not effective for distinguishing between samples of similar atomic number or between different high-pressure polymorphs, where density differences are typically on the order of a few percent.

These problems can be overcome by the use of propagation-based PCI, which has previously been shown to extend imaging studies to low-Z samples with low absorption contrast[33]. In this technique, which requires partially spatially coherent X-rays, the incident wavefront is modified by the sample’s complex refractive index i.e. both the incident wave’s phase and amplitude get modified. The amplitude change is directly accessible behind the sample by an intensity measurement; however, due to the use of hard X-rays and small sample volumes, this measurement does not necessarily contain useable information. Making use of the coherence properties of the X-rays produced by a 3rd generation synchrotron radiation source allows for the implementation of lens-less imaging methods in which the free-space propagation also encodes the phase information into measurable intensities[34,35]. This gives rise to edge enhancement contrast at small propagation distances between sample and detector i.e stronger contrast at boundaries between materials with different electron densities. PCI is used successfully at specialized beamlines to image a variety of samples from single biological cells[36] over tissue samples[37] and applications in archeology[38] or material sciences[39]. Running phase retrieval algorithms[40] on these kinds of measurements is necessary to obtain the image in the object plane, which contains quantitative information on the projected electron density of the specimen.

PCI of DAC-confined samples has previously been performed using X-ray transmission microscopy (XRTM)[41], where an objective lens assembly was placed between the sample and detector. However, although this configuration can produce a high spatial resolution on the order of 100 nm[42], it is not optimized for flux-limited studies, as the additional X-ray optics in the beam path reduce the fluence.

Here, we describe an experimental set-up developed at the P02.2 beamline at the PETRA III synchrotron radiation source which is capable of performing simultaneous time-resolved X-ray imaging and diffraction of samples in a DAC. PCI can be performed using a parallel X-ray beam, or with a compound refractive lens (CRL) focused beam with the sample positioned downstream from the X-ray focus. X-ray diffraction measurements support phase identification, structural refinement, and pressure determination using an internal diffraction standard. The capabilities of this platform are illustrated by results from dynamically-compressed Ga and Ar samples. A collection rate of 20-40 Hz for both imaging and diffraction detectors permitted the collection of images showing both melting and solidification, illustrating that the time resolution offered by this platform is suitable for kinetic studies of crystal growth. By providing *in situ* visualization of samples that are opaque to visible light, this platform has the potential to revolutionize high-pressure synchrotron studies by offering additional insight into the microscopic processes which occur inside the DAC. In addition to the dDAC driver used in this work, this experimental platform is compatible with other sample environments such as the resistively-heated DAC, opening up the possibility for its use as a melting diagnostic in future high-temperature studies.

II. Experimental Set-up

The combined imaging and diffraction set-up (Fig. 1) was constructed at the Extreme Conditions Beamline (P02.2) at PETRA III, DESY, Hamburg[2]. The set-up consists of an X-ray microscope positioned in the direct path of the X-ray beam, and two GaAs 2M LAMDBA detectors[43] positioned at either side of the imaging microscope, horizontally offset from the incident X-ray beam, for the collection of X-ray diffraction images. The microscope and LAMBDA detectors are mounted on a translation stage which permit the positioning of the entire assembly parallel to the x-ray beam, as well as in the horizontal direction perpendicular to the beam. Additional alignment of the microscope was performed using translational drives which allow for two-dimensional micro-positioning perpendicular to the X-ray beam.

The imaging microscope consists of a scintillator that is imaged onto the sensitive area of a PCO Edge 4.2 camera using a x20 objective with a working distance of 15.2 mm, a numerical aperture of 0.42, and a depth of focus of +/- 2 μm. This gives an overall magnification of x18 and a resolution limit of 0.8 μm at 550nm. A 10 μm thick cerium-doped lutetium aluminium garnet (LuAG:Ce) scintillator, which has an absorption of 12.35% at 25 keV and a peak spectral emission of > 0.9 in the 500-550 nm wavelength range, was used for all the work described here. This is well suited to work with the PCO edge 4.2 camera, which has a peak quantum efficiency of >75% in the 500-660 nm range. The choice of scintillator thickness was a trade-off between image sharpness and photon counts in the measurements. The microscope is modular and can be fitted with different imaging cameras, various objectives, and scintillators. The PCO Edge 4.2 camera allows for data collection rates up to 10 Hz at full resolution, which was suitable for the work described here. Exposure times <20 ms resulted in a reduced data quality due to flux limitations of the beamline.

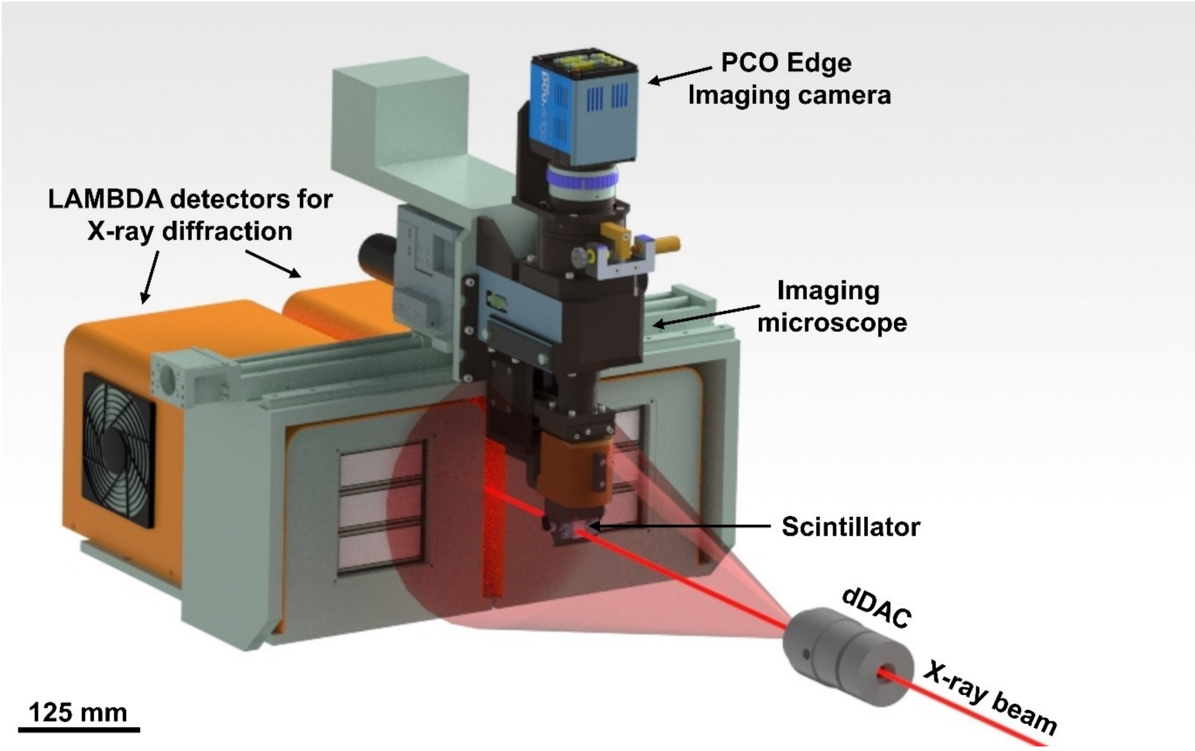

Fig. 1. Schematic showing the simultaneous X-ray imaging and diffraction set-up at the P02.2 beamline at PETRA III, where the sample is illuminated by the unfocused beam. X-ray images are collected by an X-ray microscope equipped with a 10 µm thick LuAG:Ce scintillator, a 20x objective, and a PCO Edge 4.2 camera. X-ray diffraction images are collected by two GaAs 2M LAMBDA detectors which are horizontally offset from the direct x-ray beam.

X-ray diffraction data were collected with the LAMBDA detectors in the continuous read/write mode, in which the detectors are continuously collecting with no dead time between images[43]. Synchronization of the LAMBDA detectors, PCO camera, and dDAC driver are described in Fig. 2, which is an extension of the triggering system described in ref.[10]. The PCO 4.2 camera requires a trigger signal to initiate the start of data collection for individual frames, which was provided by a square wave signal produced by an AIM-TTI function generator (TG2512A). The frequency of the trigger signal was 1000-2000 Hz; this is much higher than the data collection rate of the PCO camera and was chosen to reduce the dead time between successive images. The square wave input was gated using the output from one of the LAMBDA detectors to ensure that data collection on the LAMBDA detectors and PCO camera was started simultaneously (Fig. 3). The different trigger modes of the PCO camera and the LAMBDA detectors resulted in a small time offset between imaging and diffraction images. The time offset was on the order of several microseconds, and depended on both the exposure time of the PCO camera and the frequency of the trigger signal. The output of the LAMBDA detectors and PCO camera were therefore collected on a Tektronics MDO4000 6 GHz oscilloscope to synchronise the timing between different devices.

The experiments described here were performed using a monochromatic X-ray beam with an energy of 25.6 keV, which was chosen because GaAs sensors on the LAMBDA detectors have nearly 100% quantum efficiency at this energy. Experiments were performed in both parallel and focused beam imaging configurations. For imaging using the parallel beam, the X-ray beam was cut down to ~150(h)x150(v) μm^2 using a set of horizontal and vertical slits without any focusing optics (Fig. 4), and the PCO camera was positioned at a sample-to-detector distance of ~400 mm. Experiments were also performed in the conventional PCI configuration, where the x-ray beam was focused using 62 compound refractive lenses (CRLs) and the sample was positioned 410 mm downstream from the X-ray focus so that it was illuminated by the expanding beam (Fig. 4). In addition to the increase in flux provided by the CRLs, this also eliminates (or significantly reduces) parasitic scattering from the gasket material – especially if the illuminated area is smaller than the gasket hole. This is particularly important for diffraction diagnosis of mid- or low-Z samples, where diffraction from the gasket can easily overwhelm the sample signal.

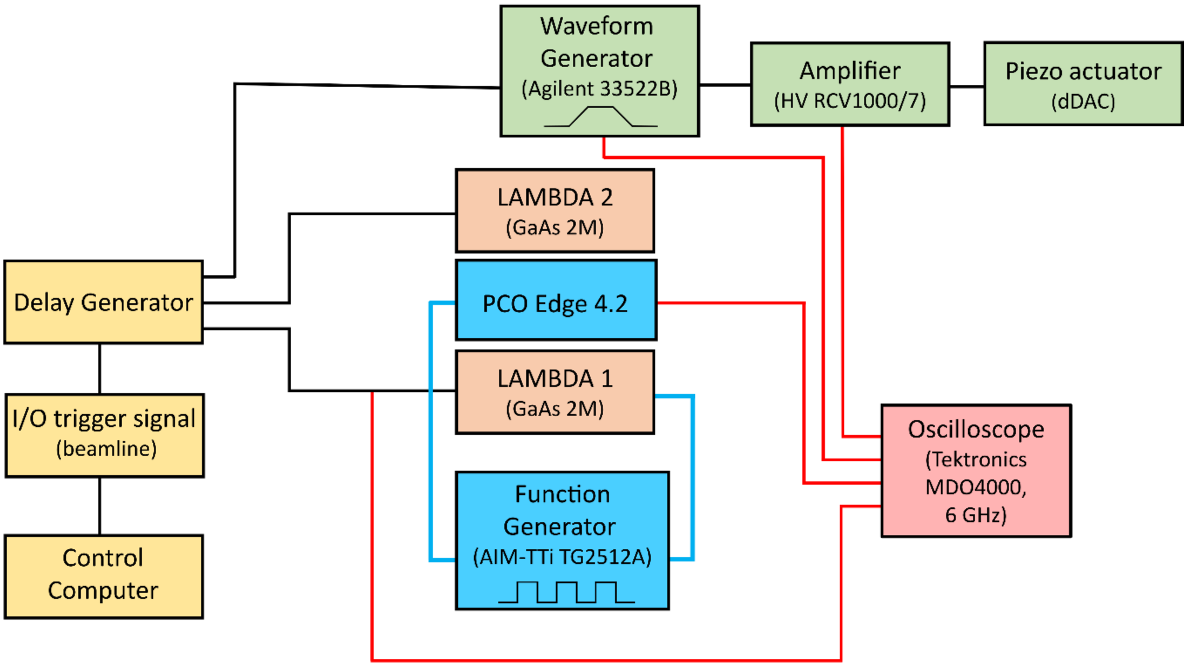

Fig. 2. Schematic of the drive control, which is employed to ensure synchronization between X-ray diffraction and imaging detectors and the dDAC driver.

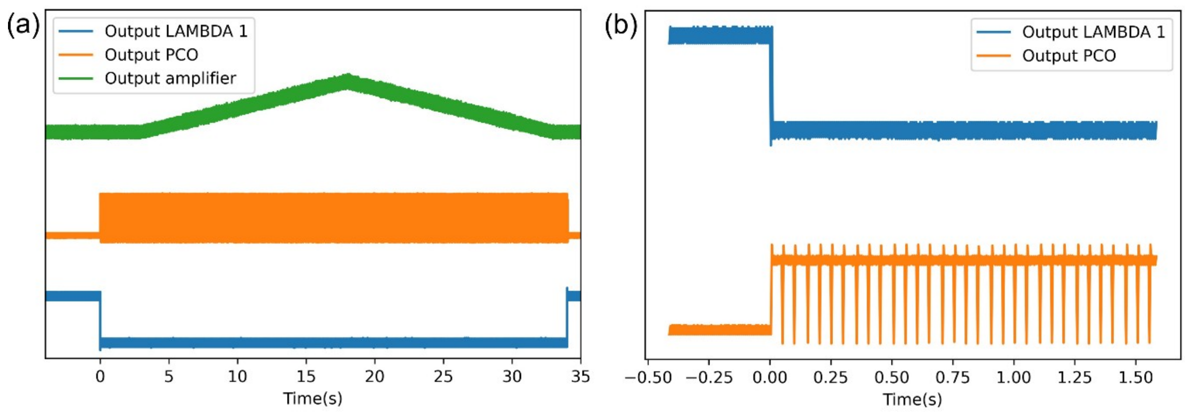

Fig. 3. (a) Outputs from LAMBDA 1, the PCO camera, and the amplifier from a typical compression ramp with a 15 s rise time. The LAMBDA output (low during collection) is used to gate the square wave input to the PCO, and the PCO output (high during collection) is used to correlate the timing of the PCO with the LAMBDA images. The oscilloscope was used in peak-detect mode to resolve voltage drops in the PCO output corresponding to the dead time between images, which results in the broad voltage signal from the amplifier. (b) Enlargement of panel (a), illustrating voltage drops following the collection of each 50 ms PCO image.

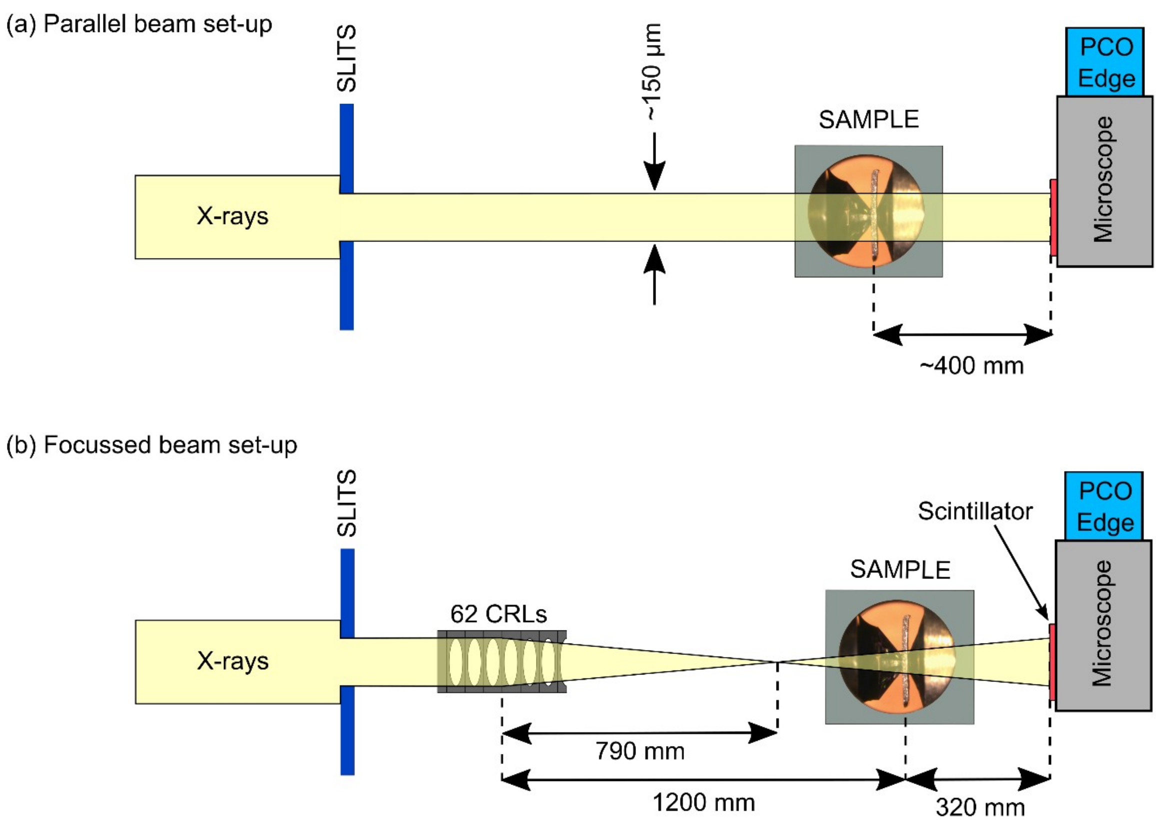

Fig. 4. Schematic showing the simultaneous imaging and diffraction set-up in the (a) parallel beam and the (b) focused beam configurations.

III. Data analysis

A. Imaging

The main challenge for image data processing is a proper correction of the flat field. The flat-field correction is the task of removing all non-signal image contributions by a division of the measured sample image by a flat image i.e. an image without sample in the beam. The structures in the flat field arise from the beamline optics, where the dominant contribution stems not only from the double crystal monochromator but also from impurities in the Be-CRLs.

Beamlines optimized for imaging usually employ stabilized monochromators, which show significantly less temporal fluctuation in the flat image. This is important for the conventional flat-field correction, since it assumes a constant flat-field. This was not the case for P02.2, as can be seen in supplementary video 1. It has been demonstrated that the flat-field fluctuations can be circumvented by employing a flat-field synthesis scheme [44]. This means that the best-fitting flat-field is calculated from an orthogonal basis of images computed by a principal component analysis (PCA) of a series of flat-field images obtained before or after the ramp. This approach yields good results for PCI even at strongly fluctuating sources like an X-ray free electron laser [45]. Transferring this scheme to dDAC imaging was only partially successful. This is due to the fact that three dynamic processes need to be separated: (i) the flat-field, (ii) the changes in the sample and (iii) the movement of the gasket or other non-sample structures in the sample chamber e.g. pressure markers or changes in the stress field of the diamond anvils. Using the scheme described above it is only possible to separate contribution (i), as (ii) and (iii) cannot be separated out. The explanation for this is that the PCA components only contain information on (i), and we cannot generate an image series which contains contributions from (ii) and (iii) in the same way they would appear during the actual compression ramp.

We therefore compute the PCA on all images including the flat-field series before and after the ramp. The resulting PCA components have to be visually inspected and are subsequently sorted in sample and non-sample contributions, where all sample contributions are then removed from the PCA basis. In most cases the sample and non-sample contributions are so different in their statistical nature that they do not appear in the same PCA component. It can still happen that (i) keeping the component as part of the basis could result in removing sample features from the corrected image since they are wrongfully attributed to the flat-field or (ii) the corrected image is contaminated by some non-sample artefacts. Reduction of the human interaction for this crucial step by improved feature extraction methods or machine learning would be a valuable improvement in future studies.

Figure 5 illustrates the processing chain using the same data shown in Fig. 7a. Panel (a) shows a raw image from a compression ramp, where the crystallites are barely visible due to structures in the empty beam. These structures can be removed by a division with a proper flat-field as shown in (b), which is achieved using the PCA components shown in (c). A total of 280 images were collected during this particular ramp, from which 40 components were extracted. For ramps at lower compression rates which produced over 2000 images, 40 components are also sufficient to describe the variations in the data set. The components which show a contribution from the sample or crystallization process have to be removed from the set of components, which are indicated by the red frames in Fig. 5(c). This then removes 16 components from the component set. The remaining components are used to describe the empty beam variations in the images by a simple matrix vector multiplication approach. The image, treated as measurement vector, is projected on the basis formed by the PCA components (treated as column vectors of the matrix) yielding the coefficients which describe the combination of components which permit the computation of the best fitting flat-field [45]. This allows us to correct for the strongly occurring fluctuations in the raw data and uncover the actual image of the processes which take place during compression in the DAC. These images could later be used to extract individual shapes of crystallites and, for example, track for example their size as function of time.

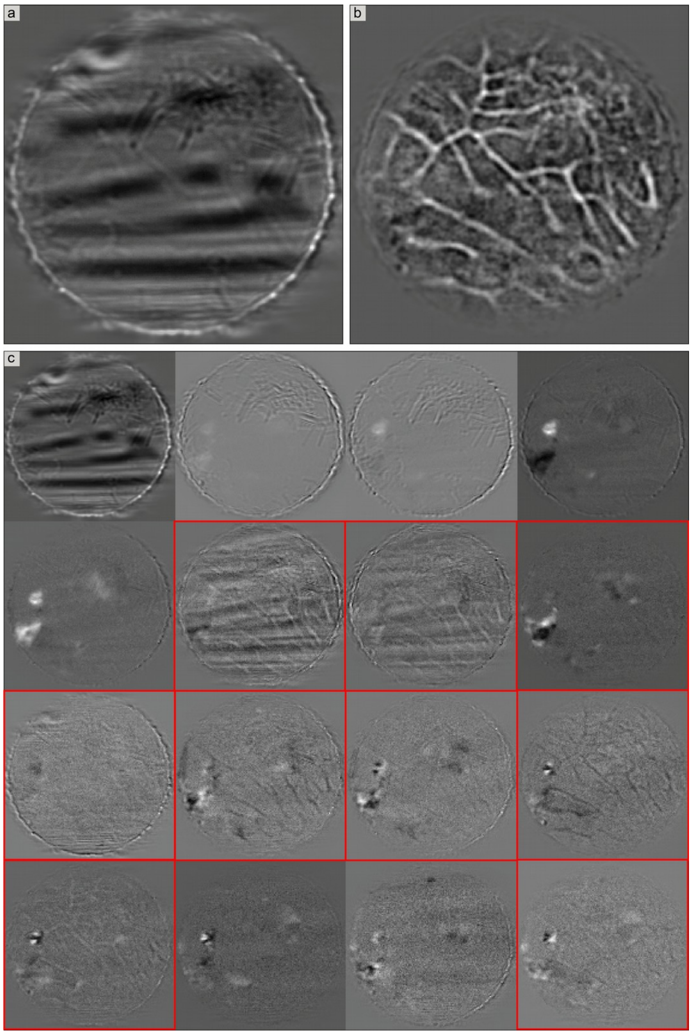

Fig. 5. Processing chain for images. (a) a raw image of the ramp during crystallization. (b) Flat-field corrected image obtained from with the PCA approach. (c) PCA components overview. Removed components are marked with a red frame. 16 out of 40 components shown. 24 components remained in the set.

B. X-ray Diffraction

Two LAMBDA detectors were calibrated using a Cr_2O_3 NIST diffraction standard where the sample-to-detector distance, detector tilt and rotation were calibrated using the DIOPTAS software[46]. The 2D diffraction images were radially-integrated using DIOPTAS to produce 1D diffraction patterns, which were further analysed using a purposely-written MATLAB code. For pressure determination, the most intense diffraction peak from the internal diffraction standard was fit using a Gaussian function and the unit cell volume was determined from the refined peak position. When Ta was used, the pressure was determined based on the peak position of the (110) reflection using the equation of state by Dewaele et al[47]. For Cu, the (111) reflection overlapped with peaks from the gasket and so pressure was determined based on the (200) reflection using the equation of state by Dewaele et al[47].

IV. Simultaneous Imaging and Diffraction experiments: Gallium

A. Motivation

Ga has an unusual phase diagram with numerous complex high-pressure polymorphs and an anomalous melting curve (Fig. 6)[7]. The orthorhombic Ga-I structure, which is stable at ambient conditions, is characterized by the coexistence of covalent and metallic bonding[48], an unusually low melting temperature of 309.2 K at ambient pressure, and a strong tendency for supercooling[49]. On compression, Ga displays a minimum in its melting curve at 275.6 K and 1.19 GPa[7], which coincides with the Ga-I/Ga-II/liquid triple point. The high-pressure Ga-II phase has a complex modulated layered structure with 104 atoms in the unit cell[50], whereas Ga-III has a simple body-centered tetragonal structure[51]. Interestingly, Ga typically does not transform to the stable Ga-II structure from the melt when compressed at room temperature. Rather, it transforms directly to metastable Ga-III[50].

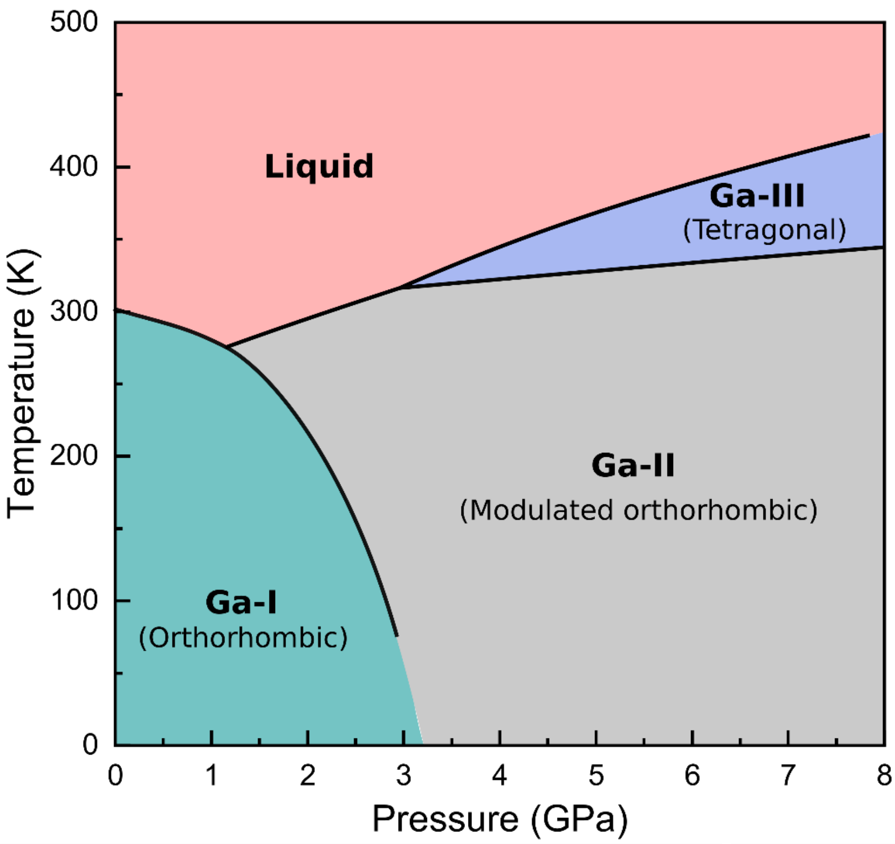

Fig. 6. Equilibrium phase diagram of Ga, modified from reference [7]. Ga transforms directly to metastable Ga-III from the liquid when compressed at room temperature, rather than to the stable Ga-II phase.

The unusual melting curve of Ga makes it uniquely suited for imaging experiments in the dDAC, as it melts and recrystallizes on compression at room temperature. This allows for the investigation of melting and solidification in liquid metals. In general, the low atomic number of Ga (Z =31) demonstrates the suitability of PCI for the study of phase transitions in mid-Z opaque materials, and how it can be used to study microscopic processes within the diamond anvil cell.

B. Sample Details

Results are presented for a total of 4 Ga samples (#1-#4), which were loaded into LLNL-type DACs[52] equipped with standard-cut diamonds with 500 μm culets and stainless-steel gaskets. No pressure transmitting medium was used. Ga easily alloys with most metals, and so samples were loaded immediately before the experiment to reduce the probability of a reaction between the Ga and the gasket material. A small grain of Ta was included as an internal pressure standard in sample #4, where Ta was chosen because it does not react or alloy with Ga at ambient temperature[53]. This was confirmed by loading Ga and Ta in a DAC at low pressures and leaving it overnight, where subsequently collected X-ray diffraction patterns showed no evidence of reaction products.

Time-resolved X-ray imaging and diffraction data of dynamically-compressed Ga were collected in both the parallel and focused beam configurations. Samples were compressed using a triangular voltage waveform with rise and fall times ranging from 5-60 s. Data were collected before and after the ramp for the creation of the time-dependent flat field correction. Each sample loading was subjected to multiple compression cycles to collect multiple data sets.

C. Experimental Results I: Parallel beam

The capabilities of the parallel X-ray beam configuration are illustrated by data collected from two Ga samples (#1 and #2) (Figs. 7 and 8), where both samples were pressurized into the liquid phase before the start of the compression ramp. Crystallization (liquid/Ga-III) was clearly visible in the X-ray images collected during a 5s compression of sample #1 (Fig. 7(a)). Solidification was proceeded by the appearance of several black spots in the X-ray images, which most likely originate from crystallites fulfilling the Bragg condition and the resultant decrease in transmitted intensity. On further compression, crystallization of Ga-III appeared to originate at the lower right-hand side of the gasket hole, and progress diagonally across the sample chamber (see supplementary video 2). The nature of the phase transition was confirmed by the simultaneous observation of mixed-phase diffraction patterns, where the integrated intensity of the diffuse scattering signal from the liquid slowly decreased as the transition progressed. Melting (Ga-III/liquid) was also clearly visible in the X-ray images collected during decompression (Fig. 7(b), supplementary video 3). Although solid/liquid phase boundaries are clearly present, interpretation of the X-ray images is complicated by overlap of features at different depths within the sample and so individual grains cannot easily be identified. This is particularly true at the onset of melting, when only a small volume of liquid has formed. Both the X-ray images and diffraction patterns show that solidification and melting occurred over similar timescales, with solidification progressing over ~10 frames (0.5 s) and melting progressed over ~52 frames (1.3 s). However, further analysis of the integrated diffraction patterns revealed the presence of several of unidentified reflections, suggesting the presence of a sample contaminant which may have influenced the phase transition process i.e. by serving as a nucleation site.

The X-ray diffraction patterns from sample #2 showed no evidence of contamination. In this sample, solidification (liquid/Ga-III) and melting (Ga-III/liquid) were very fast (<50 ms), and no mixed-phase diffraction patterns were observed (Fig. 8). Correspondingly, no evidence of solid/liquid phase boundaries or mixed phase regions were observed in the X-ray images. However, solidification could be identified by the appearance of two dark spots in the sample region in the X-ray images, similar to those observed in sample #1.

These data illustrate that, although high quality X-ray images can be collected in the parallel beam configuration, the quality of the diffraction patterns is significantly reduced by parasitic scattering from the gasket material. Although phase identification is possible, structural refinement of complex structures is not possible due to significant peak overlap. While it is possible to reduce the gasket contribution by closing the slits and illuminated area, the reduction in the field of view will mean that certain features (e.g. nucleation of a new phase initiating at the gasket) will be obscured.

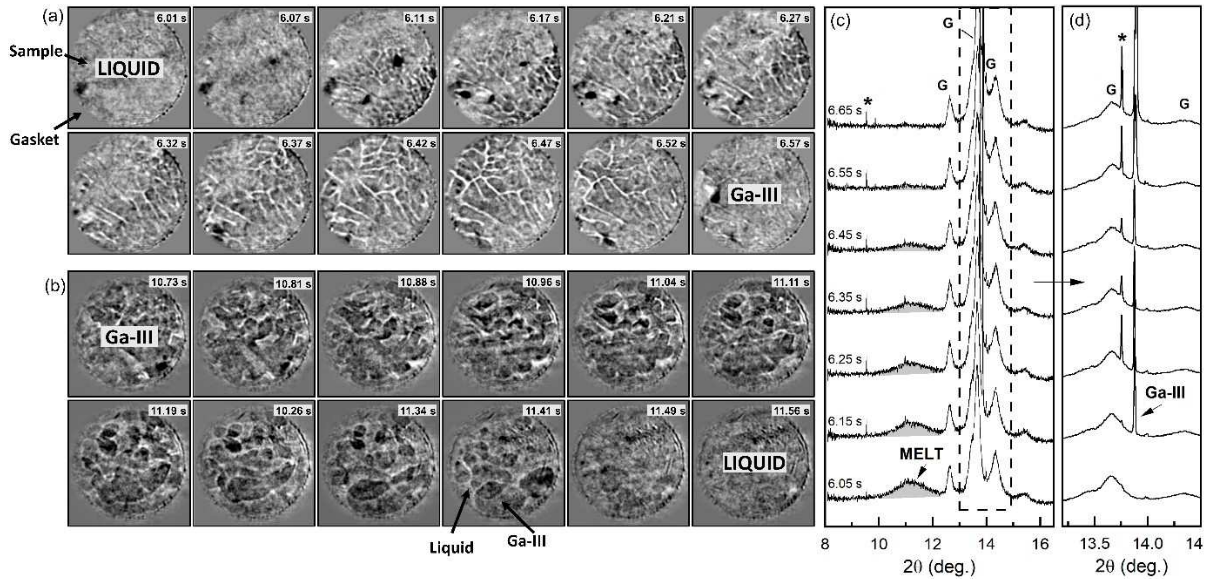

Fig. 7 X-ray images and integrated diffraction patterns collected from sample #1 (Ga) using the parallel beam configuration. (a) and (b) show crystallization (liquid/Ga-III) and melting (Ga-III/liquid) on compression and decompression, respectively, where the sample was compressed/decompressed with a 5 s rise/fall time. (a) shows every image in the series, whereas (b) shows every 3rd image. The images in (a) were collected with a 50 ms exposure time and those in (b) were collected with a 25 ms exposure time. The gasket hole (sample chamber) has a diameter of ~150μm. (c) shows the X-ray diffraction patterns corresponding to the X-ray images in (a), where each diffraction pattern was collected with an exposure time of 50 ms. In (c), the grey shaded area indicates diffuse scattering from liquid Ga. Peaks from the stainless steel gasket are indicated by G, and the asterisk indicates peaks from a contaminant phase that become more pronounced as the sample solidifies. (d) shows the same patterns as (c), but rescaled to highlight the growth of the new peak from Ga-III.

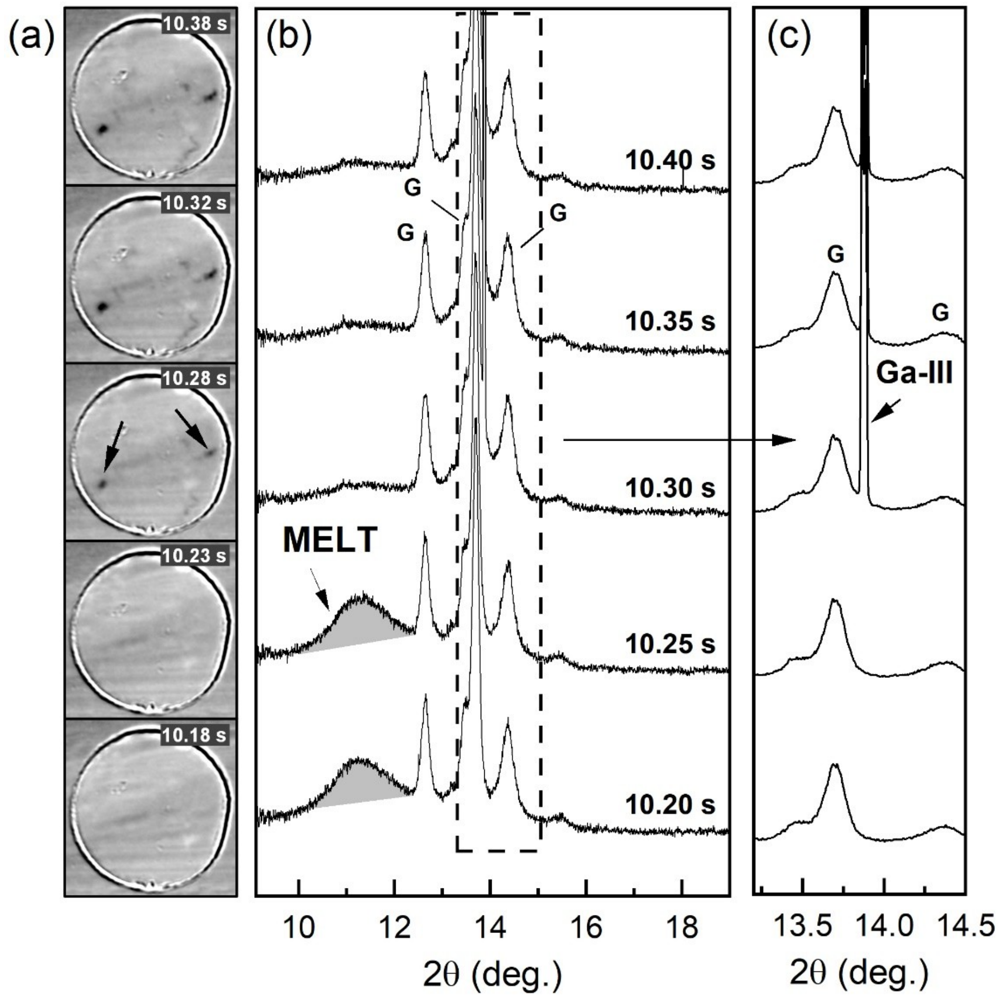

Fig. 8. (a) X-ray images and (b) integrated diffraction patterns showing the pressure-induced solidification of Ga in sample #2. Data were collected during a 15 s compression ramp using the parallel X-ray beam configuration with a 50ms exposure time for both X-ray and diffraction images. Peaks from the stainless steel gasket are indicated by G. (c) shows the same patterns as (b), but rescaled to show the growth of the Ga-III reflection. The arrows in (a) indicate the dark spots which appear when the sample is in the solid phase, which are most likely from crystallites which fulfil the Bragg condition.

D. Experimental Results II: Focused beam

The capabilities of the focused beam configuration are illustrated by data collected from two Ga samples (#3 and #4), where both imaging and diffraction data were collected using an exposure time of 50 ms (Figs 9 and 10). The samples were compressed with 60 s rise and fall times, where both melting and solidification were observed in a single compression. Solidification was easily identified based on the disappearance of diffuse scattering of the liquid. However, no reflections from the high-pressure phase were observed in either sample, which was taken as evidence of the formation of large, single-crystal like grains. Although direct structural determination was not possible, results from samples #1 and #2 and from previous studies[50] suggest that this phase corresponds to Ga-III. For both samples, the quality of both the X-ray images and diffraction patterns was significantly improved in comparison to data collected in the unfocused beam configuration. In particular, the solid/liquid phase boundaries were more clearly defined in the X-ray images, and the quality of the integrated diffraction patterns was vastly improved by a significant reduction in the parasitic scattering from the gasket.

The diffraction patterns from sample #3, which was loaded without a pressure marker, showed no evidence of sample contamination (Fig. 9(b),(d)). X-ray diffraction indicated that the Ga-I/liquid transition was a slow process proceeding over 80 frames (4 s), where melting was clearly visible in the corresponding X-ray images (Fig. 9(a), supplementary video 4). In addition to the observation of phase boundaries, solid and liquid regions could also be identified based on absorption contrast due to the density difference between the two phases, with the liquid appearing darker in the X-ray images. In contrast to melting, solidification (liquid/Ga-III) was not visible in the X-ray images, and only one mixed-phase diffraction pattern was collected. This suggests that crystallization occurred in < 50 ms (1 frame), which is significantly faster than the melting process and below the temporal resolution of these measurements.

Sample #4 was loaded with a Ta pressure marker, which enabled pressure determination over the course of the ramp (Fig. 10(c)). Small pressure drops were observed when the sample melted and recrystallized on compression, which is typical for samples undergoing a transition associated with a volume drop. Melting was similar to that in sample #3, proceeding over 90 frames (4.5 s), and there was no evidence that it originated at the Ta powder (Fig. 10(d) and Supplementary video 6). However, solidification was strikingly different than in sample #3, occurring over a much longer timescale of ~17 frames (850 ms). Solidification was clearly visible in the X-ray images (Fig. 10(e) and supplementary video 7), and indicated two distinct growth processes which occurred over two different timescales. Firstly, the initial growth of large crystals of Ga-III occurred during the collection of a single X-ray image, indicated a growth time of <50 ms. Subsequent growth was much slower, with very little change in the crystal size or shape between subsequent images.

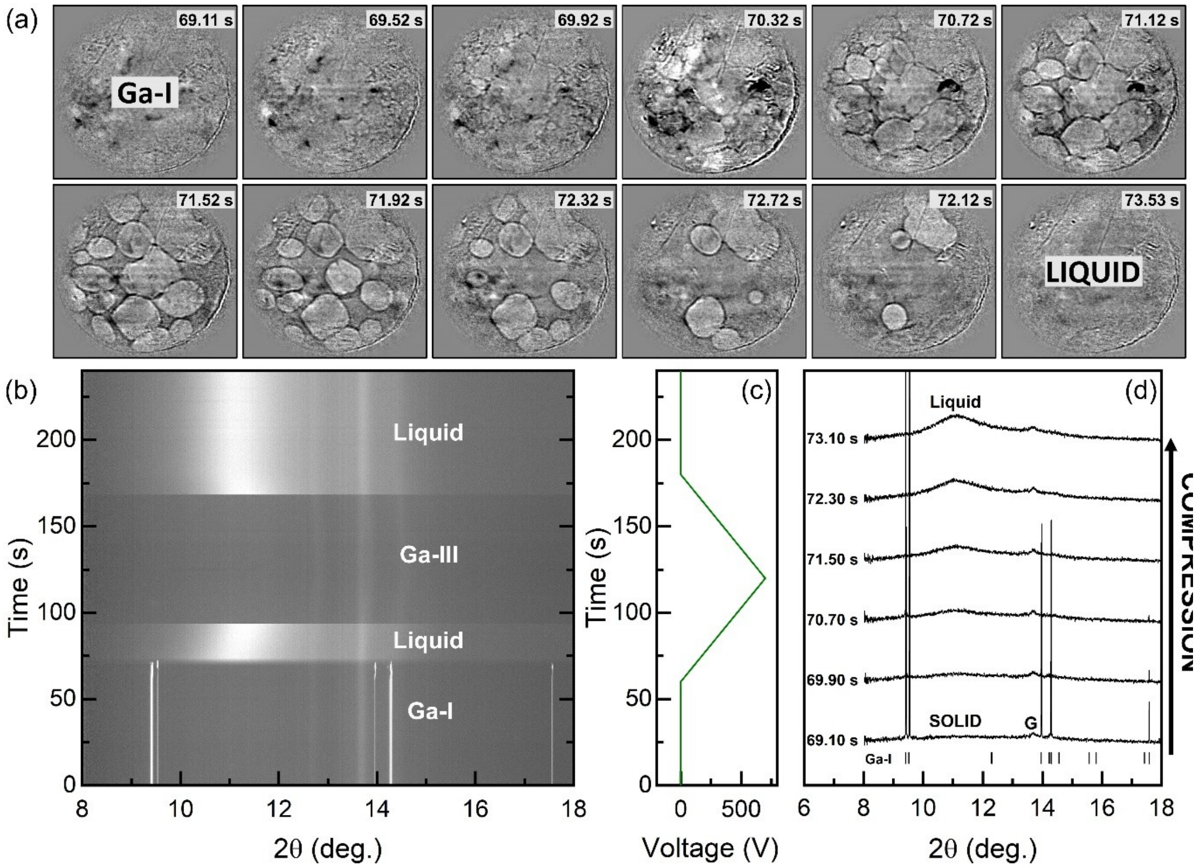

Fig. 9. X-ray images and integrated diffraction patterns showing the melting (Ga-I to liquid) of Ga on compression, where data were collected using the focused beam set-up (supplementary video 4). Data were collected from sample #3, which was loaded without a pressure marker into a gasket hole with a diameter of ~150μm. (a) Flat field corrected X-ray images which were collected with a 50 ms exposure time, where only every 8th image is shown. (b) Intensity plot showing time-dependent changes in the integrated diffraction patterns over the entire ramp. (c) Applied voltage waveform. (d) Integrated diffraction patterns collected with a 50 ms exposure time, where only every 8th image is shown.

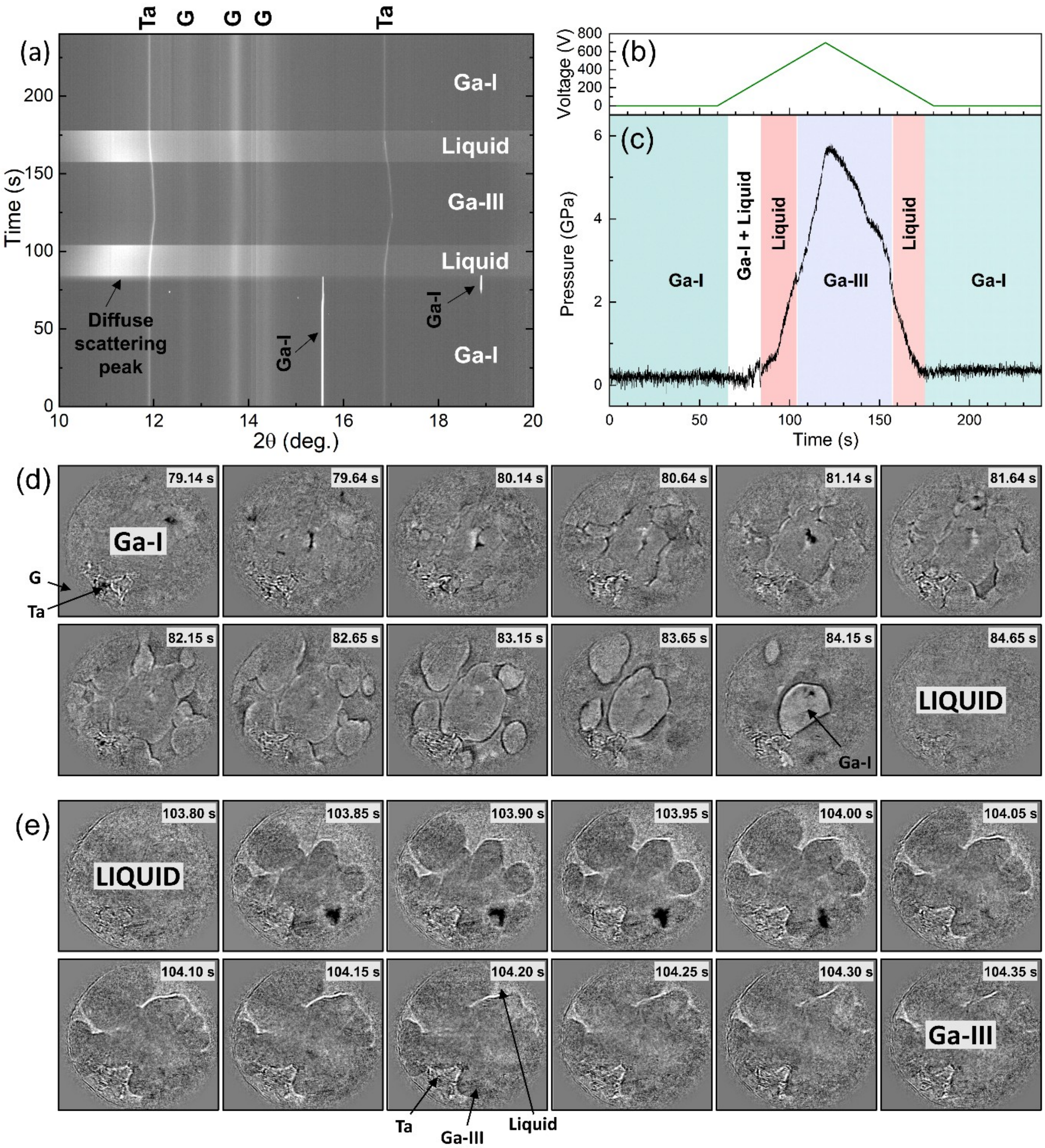

Fig. 10. (a) Intensity plot showing the time evolution of the X-ray diffraction images collected during the compression of sample #4 (Ga+Ta). Ta indicates reflections from the Ta pressure marker, whereas G indicates reflections from the gasket. (b) Compression ramp applied to the sample. (c) Time-dependent pressure profile during the compression ramp, as determined from the unit cell volume of the Ta pressure marker. (d) and (e) X-ray images showing melting (Ga-I/liquid) and solidification (liquid/Ga-III) during the compression ramp, respectively (supplementary videos 6 and 7). Images were collected using a 50 ms exposure time. (a) shows every 10^{th} image, whereas (b) shows every image in the series. The gasket hole (sample chamber) has a diameter of ~150µm.

V. Simultaneous Imaging and Diffraction experiments: Argon

A. Motivation

Ar, a noble gas with atomic number 18, crystallizes in the fcc phase at 1.4 GPa when compressed in the DAC at room temperature[54]. Ar is sometimes used as a pressure-transmitting medium, although not as frequently as Ne and He for which the effects of non-hydrostaticity occur at higher pressures[54]. Ar is also often used as an insulator for laser-heating experiments[55,56], i.e. as a thermal boundary layer between the sample and the diamond anvil. The phase diagram is shown in Fig. 11, which indicates the pressure path taken during dDAC compression.

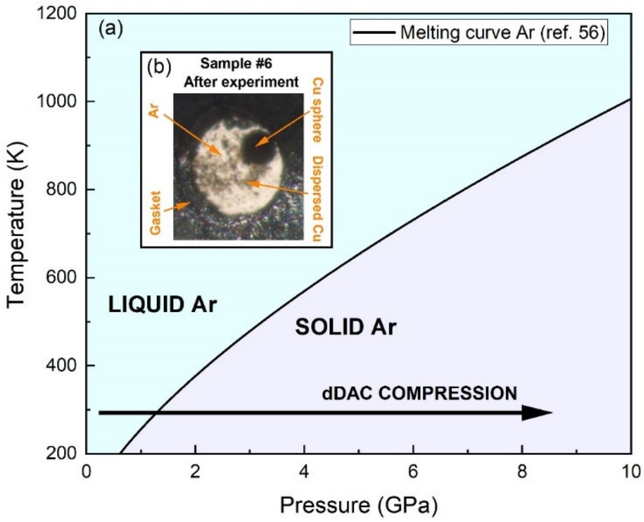

Fig. 11. (a) Phase diagram of Ar, modified from reference [57]. The arrow shows the pressure path experienced by the sample during the dDAC compression. (b) Photomicrograph of sample #6 after the experiment, showing the dispersed Cu particles around the sample chamber which originated from the Cu sphere which was added as a pressure marker.

B. Sample details

A total of 2 Ar samples (#5 and #6) were loaded into LLNL-type DACs[52] using the in-house gas loading system at LLNL, where the DACs were equipped with standard-cut diamonds with 500 μm culets and stainless-steel gaskets. No pressure marker was used in sample #5, whereas a Cu sphere was added to sample #6 as an internal pressure standard. X-ray imaging and diffraction data were collected in the focused beam configuration using an exposure time of 20-50ms for both imaging and diffraction detectors. The samples were dynamically-compressed using a triangular voltage waveform with rise (fall) times ranging from 1-60s, and each sample loading was subjected to multiple compression cycles to collect multiple data sets. Data were collected before and after each of the compression cycle to create the time-varying flat-field correction for X-ray image analysis.

C. Experimental Results: Focused beam

Sample #5, which consisted of Ar loaded without a pressure marker, was compressed a total of 4 times through the liquid/solid transition with rise times ranging from 1-60s. After each of the runs, the sample remained in the solid phase following decompression and the pressure had to be manually lowered before the start of the next ramp. No evidence of crystallization was observed in the X-ray images collected on compression during any of the runs. Weak Ar reflections were observed in the X-ray diffraction patterns collected from pressures of ~4 GPa on compression, which is higher than the Ar solidification pressure. These were identified to originate from diffraction spots in the 2D diffraction images, rather than from smooth Debye Scherrer rings. The Ar reflections became much more intense on decompression, which was accompanied by an increase in the number of diffraction spots observed on the 2D diffraction images. This was particularly pronounced for the 10s compression ramp (Fig. 12), where no Ar reflections were observed on LAMBDA1 during compression, but appeared at the onset of decompression at ~10 GPa. Diffuse scattering from Ar was not clearly visible in the integrated diffraction patterns, which prevented the determination of the onset solidification pressure based on the disappearance of the liquid phase.

The first observation of Ar reflections above the solidification pressure is most likely due the formation of large, single-crystal like Ar gains which do not initially fulfil the Bragg condition, which is consistent with the spotty nature of the Ar diffraction patterns. This is consistent with the results from previous studies in which Ar was observed to form single crystals when compressed from the melt[52]. The pronounced increase in the diffracted signal from solid Ar on decompression is most likely due to the breakdown of the large grains into a larger number of small crystallites with different orientations that contribute to the diffraction signal. Consequently, it is not possible to determine the transition pressure or transition timescale based on the X-ray diffraction data. However, the absence of crystallization in the X-ray images suggests that the transition is too fast to be observed on these timescales (exposure times of 20-50 ms).

Sample #6, which was loaded with a Cu ball embedded in an Ar media, was compressed a total of 7 times through the liquid/solid transition with rise times ranging from 1-240s. No evidence of crystallization was observed in the X-ray images collected during the initial 60s compression, similar to what was observed in sample #5. However, the X-ray images collected in subsequent runs showed clear evidence of both crystallization and melting (Fig. 13 and supplementary videos 8 and 9). On compression, crystallization was identified by the appearance of a dense network of dark spots, which we identified as the formation of large number of small crystallites. This was confirmed by the appearance of Ar reflections in the corresponding X-ray diffraction patterns at 1.6 GPa. Melting was identified by the appearance of solid/liquid phase boundaries, which became more pronounced as the transition progressed. Crystallization proceeded over ~11 X-ray images (550 ms), and was slightly faster than melting, which proceeded over ~8 images (400 ms).

The striking difference in the crystallization process in samples #5 and #6 was surprising, as it was not initially clear why the inclusion of the large Cu sphere resulted in the formation of a large number of small crystallites. However, visual observation of the sample under the microscope after the experiment revealed that small grains of Cu were dispersed throughout the sample chamber (Fig. 11(b)), which may have acted as nucleation sites which facilitated the growth of a large number of small Ar crystallites with different orientations. The fact that crystallization was not observed during the initial compression of sample #6 suggests that the dislodging of Cu grains first occurred during sample melting on decompression.

The observation of longer transition timescales in sample #6 was initially surprising, as the presence of a large number of nucleation sites would be expected to result in a faster transition time than for the pure sample. However, as it was not possible to determine the transition pressure in the case of pure Ar (sample #6), the possibility that liquid Ar was over-pressurized above the equilibrium phase boundary cannot be ruled out. Over-pressurization would result in a smaller activation energy, which would be expected to result in a faster transition. Further investigation is required to determine the transition pressures in pure Ar samples, where care must be taken to ensure that the method of pressure determination does not influence the transition.

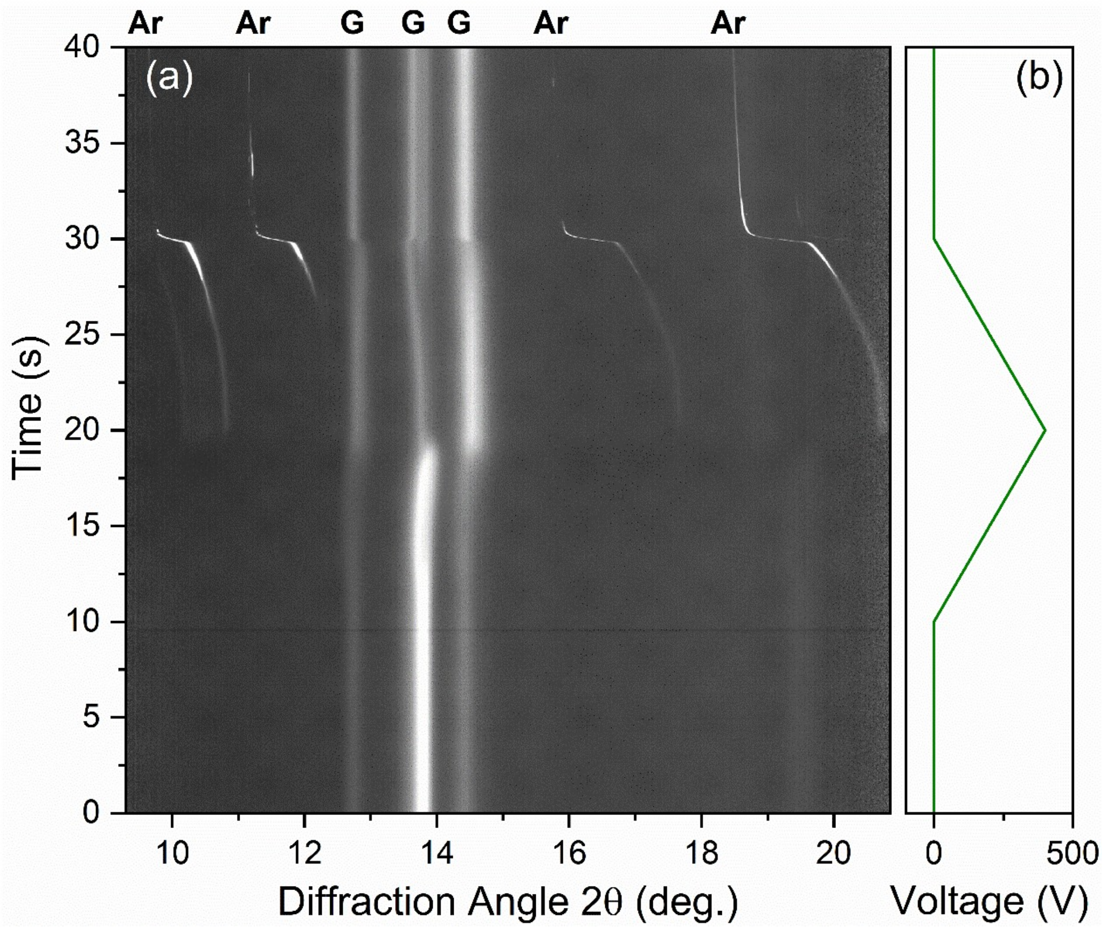

Fig. 12. (a) Intensity plot showing the time-dependent changes in the integrated diffraction patterns collected from LAMBDA 1 during a 10s compression of sample #5, which consisted of Ar loaded without a pressure marker. (b) shows the corresponding voltage waveform. Reflections from the Ar sample are indicated by **Ar**, whereas reflections from the stainless steel gasket are indicated by **G**. Reflections from solid Ar were not observed on compression, but instead appeared at the onset of decompression at ~10 GPa. A single, weak Ar reflection was observed on LAMBDA 2 from ~4 GPa.

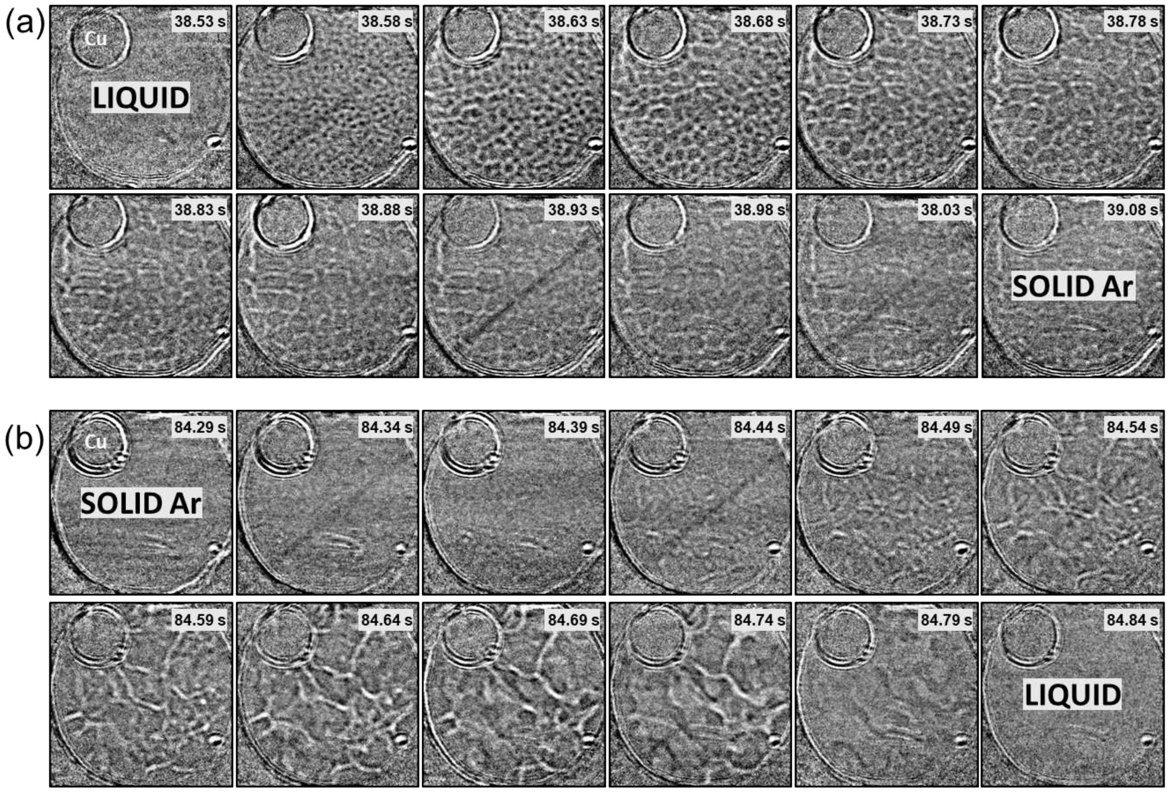

Fig. 13. X-ray images collected from sample #6, which shows (a) crystallization and (b) melting of Ar (sample #6) on compression and decompression, respectively, during a compression cycle with 30s rise and fall times (supplementary videos 8 and 9). The gasket hole (sample chamber) has a diameter of ~150µm, and this sample was loaded with a Cu sphere for pressure determination. Data were collected with an exposure time of 50 ms, and the panels in (a) and (b) both show consecutive image collected during the compression/decompression cycle.

E. Discussion

We have successfully demonstrated that PCI can be used to visualize phase transitions in elemental materials compressed using the dDAC. Edge-enhancement produced by the partially coherent X-ray beam produces strong contrast at liquid/solid phase boundaries, which are clearly visible in the X-ray images collected from samples undergoing phase transitions. X-ray images showing melting and solidification have been successfully collected using both the parallel beam and focused X-ray beam set-ups for two different material systems: Ga and Ar. X-ray images collected from Ga are particularly striking, as phase boundaries in metallic systems cannot be visualized using optical imaging. We note that the difference in electron density between two different high-pressure phases of a given material (i.e. between liquid and solid) is smaller than the difference in electron density between two chemically distinct materials, and so we expect PCI will produce high quality images with strong contrast for mixtures of materials with different compositions.

X-ray images were collected from Ga using both the unfocused and focused beam set-ups, allowing us to make a comparison between the two experimental configurations. Overall, the quality of the data collected using the focused beam was higher than for those collected using the parallel beam, with the additional advantage that it produces ‘clean’ diffraction patterns without gasket contribution. However, although the collection times were comparable for all of the experimental runs, the timescale of the compression ramps applied to samples #1 and #2 (parallel beam) were much faster (5-15s) than those applied to samples #3 and #4 (focused beam, 60s ramp). The possibility that the increased speed of crystal growth in the faster compression ramp resulted in enhanced time-blurring in the images therefore cannot be ruled out. In addition, the samples #1 and #2 started already in the liquid phase, and so images from the Ga-I/liquid transition could not be collected. Instead, melting was observed during the Ga-III/liquid transition on decompression, which is expected to show lower contrast than Ga-I /liquid due to the smaller volume drop associated with the transition[58].

The results from these experiments also demonstrate how X-ray imaging can allow us to gain insight into phase transitions. In the case of Ga, the presence of a sample contaminant or the inclusion of an internal pressure standard resulted in longer melting and solidification times in comparison to pure Ga. This was particularly striking for solidification, which was not observed in X-ray images collected from pure Ga. The same is true for Ar, where solidification was only observed in the X-ray images collected from sample #5, which was loaded with a pressure marker. In this case, crystallization was most likely influenced by a small amount of dispersed Cu powder, which may have acted as nucleation sites for crystallization.

F. Outlook

The ability to perform imaging experiments at extreme *P*-*T* conditions will be an invaluable tool for many areas of research within high pressure science. In particular, as it can potentially be coupled with a range of sample environments such as resistive and laser heating techniques or cryostat systems, which allow for samples to be studied over a large region of P-T space. The extension of dynamic compression experiments to higher temperatures using a resistively-heated dDAC[59] offers the opportunity to extend the study of melting and solidification to materials with melting temperatures up to ~1400 K, whereas imaging of laser heated samples offers the opportunity to extend particle tracking studies[24] to samples that are opaque to visible light. In general, the ability to visualize a sample in the vicinity of its melting curve can provide additional information on the melting process, particularly for samples in which the melting temperature is subject to intense debate[60–62]. Imaging can also provide information on phase mixability, which is important for planetary modelling. For example, it has been proposed that the excess luminosity of Saturn can be explained by hydrogen and helium de-mixing in the planetary interior[63], where latent heat and gravitational energy of sinking He droplets act as an energy source[64].

The significantly increased X-ray coherence of 4th generation synchrotron radiation sources such as the ESRF and the planned upgrades to PETRA IV and APS-U will offer the opportunity for phase reconstruction from PCI images. In addition, the increase in flux will allow for full data collection at faster frame rates, which will allow synchrotron dDAC imaging studies to be extended to faster compression rates. In addition, high-energy XFEL sources such as the European XFEL (EuXFEL), which has a dedicated DAC setup at the HED instrument, may be used to extend dDAC studies to even faster compression rates[65]. The pulse train structure of the EuXFEL provides an unparalleled time resolution up 4.5 MHz, where the short timescale of the femtosecond XFEL pulses will avoid time blurring by providing a snapshot of the sample during the compression ramp.

G. Conclusions

This work describes an experimental platform at the Extreme Conditions Beamline (P02.2) at the PETRA III synchrotron radiation source at DESY, Hamburg, which is capable of collecting simultaneous X-ray imaging and diffraction data from samples that are compressed in the piezo-driven DAC. This set-up can perform PCI using both an unfocused and focused X-ray beam, where the focused beam configuration resulted in both an improvement in the X-ray images and a reduction in parasitic scattering in the diffraction patterns. The capabilities of this platform are illustrated by dynamic compression experiments on Ga and Ar, where melting and crystallization were clearly identified by the appearance of solid/liquid phase boundaries in the X-ray images collected during the transition, demonstrating the suitability of PCI for the observation of pressure-induced phase transitions in elemental materials. This platform is compatible with different sample environments and DAC drivers, making it compatible with a range of experimental measurements such as melt curve determination.

Supplementary Material

See supplementary material for videos showing the fluctuations of the X-ray beam caused by instabilities in the beamline's optics (supplementary video 1) and videos showing the X-ray images and corresponding integrated diffraction patterns collected during melting and crystallization of Ga samples #1, #3 and #4 (supplementary videos 2-7) and Ar samples #6 (supplementary videos 8-9).

Acknowledgments

We acknowledge DESY (Hamburg, Germany), a member of the Helmholtz Association HGF, for the provision of experimental facilities. Parts of this research were carried out at beamline P02.2 at PETRA III, and we thank M.W. and S.W. for technical support at the beamline. Portions of this work (Zs.J., E.F.O., D.T.S., M.J.L. and W.J.E.) were performed under the auspices of the US Department of Energy by Lawrence Livermore National Laboratory under Contract No. DE-AC52-07NA27344.

Conflict of Interest

The authors have no conflicts to disclose.

Data Availability

The data that support the findings of this study are available from the corresponding author upon reasonable request.

References

[1] G. Shen, P. Chow, Y. Xiao, S. Sinogeikin, Y. Meng, W. Yang, H.-P. Liermann, O. Shebanova, E. Rod, A. Bommannavar, and H.-K. Mao, High Press. Res. **28**, 145 (2008).
[2] H.-P. Liermann, Z. Konôpková, W. Morgenroth, K. Glazyrin, J. Bednarčik, E.E. McBride, S. Petitgirard, J.T. Delitz, M. Wendt, Y. Bican, A. Ehnes, I. Schwark, A. Rothkirch, M. Tischer, J. Heuer, H. Schulte-Schrepping, T. Kracht, and H. Franz, J. Synchrotron Radiat. **22**, 908 (2015).
[3] T. Connolley, C.M. Beavers, and P. Chater, Synchrotron Radiat. News **33**, 31 (2020).
[4] M.I. McMahon and R.J. Nelmes, Chem. Soc. Rev. **35**, 943 (2006).
[5] Y. Ma, M. Eremets, A.R. Oganov, Y. Xie, I. Trojan, S. Medvedev, A.O. Lyakhov, M. Valle, and V. Prakapenka, Nature **458**, 182 (2009).
[6] C.L. Guillaume, E. Gregoryanz, O. Degtyareva, M.I. McMahon, M. Hanfland, S. Evans, M. Guthrie, S.V. Sinogeikin, and H.-K. Mao, Nat. Phys. **7**, 211 (2011).
[7] A. Jayaraman, W. Klement, R.C. Newton, and G.C. Kennedy, J. Phys. Chem. Solids **24**, 7 (1963).
[8] N. Nishiyama, S. Seike, T. Hamaguchi, T. Irifune, M. Matsushita, M. Takahashi, H. Ohfuji, and Y. Kono, Scr. Mater. **67**, 955 (2012).
[9] W.J. Evans, C.-S. Yoo, G.W. Lee, H. Cynn, M.J. Lipp, and K. Visbeck, Rev. Sci. Instrum. **78**, 073904 (2007).
[10] Zs. Jenei, H.P. Liermann, R. Husband, A.S.J. Méndez, D. Pennicard, H. Marquardt, E.F. O'Bannon, A. Pakhomova, Z. Konopkova, K. Glazyrin, M. Wendt, S. Wenz, E.E. McBride, W. Morgenroth, B. Winkler, A. Rothkirch, M. Hanfland, and W.J. Evans, Rev. Sci. Instrum. **90**, 065114 (2019).
[11] G.W. Lee, W.J. Evans, and C.-S. Yoo, Phys. Rev. B **74**, 134112 (2006).
[12] G.W. Lee, W.J. Evans, and C.-S. Yoo, Proc. Natl. Acad. Sci. **104**, 9178 (2007).
[13] J.-Y. Chen and C.-S. Yoo, Proc. Natl. Acad. Sci. **108**, 7685 (2011).
[14] D.A. Tomasino and C.S. Yoo, J. Phys. Conf. Ser. **500**, 032019 (2014).
[15] R.J. Husband, E.F. O'Bannon, H.-P. Liermann, M.J. Lipp, A.S.J. Méndez, Z. Konôpková, E.E. McBride, W.J. Evans, and Z. Jenei, Sci. Rep. **11**, 14859 (2021).
[16] Y.-J. Kim, Y.-H. Lee, S. Lee, H. Nada, and G.W. Lee, Proc. Natl. Acad. Sci. **116**, 8679 (2019).
[17] A.S.J. Méndez, F. Trybel, R.J. Husband, G. Steinle-Neumann, H.-P. Liermann, and H. Marquardt, Phys. Rev. B **103**, 064104 (2021).
[18] H. Marquardt, J. Buchen, A.S.J. Mendez, A. Kurnosov, M. Wendt, A. Rothkirch, D. Pennicard, and H.-P. Liermann, Geophys. Res. Lett. **45**, 6862 (2018).
[19] M. van Kan Parker, C. Sanloup, N. Sator, B. Guillot, E.J. Tronche, J.-P. Perrillat, M. Mezouar, N. Rai, and W. van Westrenen, Nat. Geosci. **5**, 186 (2012).
[20] B. Chen, L. Gao, K. Leinenweber, Y. Wang, T. Sanehira, and J. Li, High Press. Res. **28**, 315 (2008).
[21] K. Mibe, M. Kanzaki, T. Kawamoto, K.N. Matsukage, Y. Fei, and S. Ono, J. Geophys. Res. Solid Earth **112**, (2007).
[22] T. Kawamoto, M. Kanzaki, K. Mibe, K.N. Matsukage, and S. Ono, Proc. Natl. Acad. Sci. **109**, 18695 (2012).
[23] J. Guignard and W.A. Crichton, Rev. Sci. Instrum. **86**, 085112 (2015).
[24] H.B. Bartlett, N. Gomez-Perez, M. Hermes, and R.S. McWilliams, Phys. Rev. B **101**, 144202 (2020).
[25] M. Kanzaki, K. Kurita, T. Fujii, T. Kato, O. Shimomura, and S. Akimoto, in *High-Press. Res. Miner. Phys. Vol. Honor Syun-Iti Akimoto* (American Geophysical Union (AGU), 1987), pp. 195–200.
[26] Y. Kono, C. Kenney-Benson, C. Park, G. Shen, and Y. Wang, Phys. Rev. B **87**, 024302 (2013).
[27] Y. Kono, C. Kenney-Benson, D. Hummer, H. Ohfuji, C. Park, G. Shen, Y. Wang, A. Kavner, and C.E. Manning, Nat. Commun. **5**, 5091 (2014).
[28] H. Spice, C. Sanloup, B. Cochain, C. de Grouchy, and Y. Kono, Geochim. Cosmochim. Acta **148**, 219 (2015).
[29] Y. Kono, C. Kenney-Benson, Y. Shibazaki, C. Park, G. Shen, and Y. Wang, Phys. Earth Planet. Inter. **241**, 57 (2015).
[30] Y. Kono, in *Magmas Press.*, edited by Y. Kono and C. Sanloup (Elsevier, 2018), pp. 261–280.
[31] W.L. Mao, Y. Lin, Y. Liu, and J. Liu, Engineering **5**, 479 (2019).
[32] A. Momose, Jpn. J. Appl. Phys. **44**, 6355 (2005).
[33] Y. Kono, C. Kenney-Benson, Y. Shibazaki, C. Park, Y. Wang, and G. Shen, Rev. Sci. Instrum. **86**, 072207 (2015).

[34] S.W. Wilkins, T.E. Gureyev, D. Gao, A. Pogany, and A.W. Stevenson, Nature **384**, 335 (1996).
[35] P. Cloetens, R. Barrett, J. Baruchel, J.-P. Guigay, and M. Schlenker, J. Phys. Appl. Phys. **29**, 133 (1996).
[36] J.-D. Nicolas, J. Hagemann, M. Sprung, and T. Salditt, J. Synchrotron Radiat. **25**, 1196 (2018).
[37] M. Töpperwien, F. van der Meer, C. Stadelmann, and T. Salditt, Proc. Natl. Acad. Sci. **115**, 6940 (2018).
[38] P. Tafforeau, R. Boistel, E. Boller, A. Bravin, M. Brunet, Y. Chaimanee, P. Cloetens, M. Feist, J. Hoszowska, J.-J. Jaeger, R.F. Kay, V. Lazzari, L. Marivaux, A. Nel, C. Nemoz, X. Thibault, P. Vignaud, and S. Zabler, Appl. Phys. A **83**, 195 (2006).
[39] S. Meyer, A. Wolf, D. Sanders, K. Iskhakova, H. Ćwieka, S. Bruns, S. Flenner, I. Greving, J. Hagemann, R. Willumeit-Römer, B. Wiese, and B. Zeller-Plumhoff, Metals **11**, 1422 (2021).
[40] D.R. Luke, J.V. Burke, and R.G. Lyon, SIAM Rev. **44**, 169 (2002).
[41] T. Fedotenko, L. Dubrovinsky, G. Aprilis, E. Koemets, A. Snigirev, I. Snigireva, A. Barannikov, P. Ershov, F. Cova, M. Hanfland, and N. Dubrovinskaia, Rev. Sci. Instrum. **90**, 104501 (2019).
[42] A. Bosak, I. Snigireva, K.S. Napolskii, and A. Snigirev, Adv. Mater. **22**, 3256 (2010).
[43] D. Pennicard, S. Smoljanin, B. Struth, H. Hirsemann, A. Fauler, M. Fiederle, O. Tolbanov, A. Zarubin, A. Tyazhev, G. Shelkov, and H. Graafsma, J. Instrum. **9**, C12026 (2014).
[44] V.V. Nieuwenhove, J.D. Beenhouwer, F.D. Carlo, L. Mancini, F. Marone, and J. Sijbers, Opt. Express **23**, 27975 (2015).
[45] J. Hagemann, M. Vassholz, H. Hoeppe, M. Osterhoff, J.M. Rosselló, R. Mettin, F. Seiboth, A. Schropp, J. Möller, J. Hallmann, C. Kim, M. Scholz, U. Boesenberg, R. Schaffer, A. Zozulya, W. Lu, R. Shayduk, A. Madsen, C.G. Schroer, and T. Salditt, J. Synchrotron Radiat. **28**, 52 (2021).
[46] C. Prescher and V.B. Prakapenka, High Press. Res. **35**, 223 (2015).
[47] A. Dewaele, P. Loubeyre, and M. Mezouar, Phys. Rev. B **70**, 094112 (2004).
[48] M. Bernasconi, G.L. Chiarotti, and E. Tosatti, Phys. Rev. B **52**, 9988 (1995).
[49] L. Bosio, A. Defrain, and I. Epelboin, J. Phys. **27**, 61 (1966).
[50] O. Degtyareva, M.I. McMahon, D.R. Allan, and R.J. Nelmes, Phys. Rev. Lett. **93**, 205502 (2004).
[51] L. Bosio, J. Chem. Phys. **68**, 1221 (1978).
[52] Z. Jenei, H. Cynn, K. Visbeck, and W.J. Evans, Rev. Sci. Instrum. **84**, 095114 (2013).
[53] Y. Fujinaga and Y. Murakami, Mater. Trans. **44**, 377 (2003).
[54] S. Klotz, J.-C. Chervin, P. Munsch, and G.L. Marchand, J. Phys. Appl. Phys. **42**, 075413 (2009).
[55] A.F. Goncharov, V.B. Prakapenka, V.V. Struzhkin, I. Kantor, M.L. Rivers, and D.A. Dalton, Rev. Sci. Instrum. **81**, 113902 (2010).
[56] Z. Du, T. Gu, V. Dobrosavljevic, S.T. Weir, S. Falabella, and K.K.M. Lee, Rev. Sci. Instrum. **86**, 095103 (2015).
[57] F. Datchi, P. Loubeyre, and R. LeToullec, Phys. Rev. B **61**, 6535 (2000).
[58] R. Li, L. Li, T. Yu, L. Wang, J. Chen, Y. Wang, Z. Cai, J. Chen, M.L. Rivers, and H. Liu, Appl. Phys. Lett. **105**, 041906 (2014).
[59] A.S.J. Méndez, H. Marquardt, R.J. Husband, I. Schwark, J. Mainberger, K. Glazyrin, A. Kurnosov, C. Otzen, N. Satta, J. Bednarcik, and H.-P. Liermann, Rev. Sci. Instrum. **91**, 073906 (2020).
[60] R. Boehler, Nature **363**, 534 (1993).
[61] S. Anzellini, A. Dewaele, M. Mezouar, P. Loubeyre, and G. Morard, Science **340**, 464 (2013).
[62] G. Morard, S. Boccato, A.D. Rosa, S. Anzellini, F. Miozzi, L. Henry, G. Garbarino, M. Mezouar, M. Harmand, F. Guyot, E. Boulard, I. Kantor, T. Irifune, and R. Torchio, Geophys. Res. Lett. **45**, 11,074 (2018).
[63] S. Brygoo, P. Loubeyre, M. Millot, J.R. Rygg, P.M. Celliers, J.H. Eggert, R. Jeanloz, and G.W. Collins, Nature **593**, 517 (2021).
[64] M.A. Morales, E. Schwegler, D. Ceperley, C. Pierleoni, S. Hamel, and K. Caspersen, Proc. Natl. Acad. Sci. **106**, 1324 (2009).
[65] H.P. Liermann, Z. Konôpková, K. Appel, C. Prescher, A. Schropp, V. Cerantola, R.J. Husband, J.D. McHardy, M.I. McMahon, R.S. McWilliams, C.M. Pépin, J. Mainberger, M. Roeper, A. Berghäuser, H. Damker, P. Talkovski, M. Foese, N. Kujala, O.B. Ball, M.A. Baron, R. Briggs, M. Bykov, E. Bykova, J. Chantel, A.L. Coleman, H. Cynn, D. Dattelbaum, L.E. Dresselhaus-Marais, J.H. Eggert, L. Ehm, W.J.

Evans, G. Fiquet, M. Frost, K. Glazyrin, A.F. Goncharov, H. Hwang, Z. Jenei, J.-Y. Kim, F. Langenhorst, Y. Lee, M. Makita, H. Marquardt, E.E. McBride, S. Merkel, G. Morard, E.F. O'Bannon, C. Otzen, E.J. Pace, A. Pelka, J.S. Pigott, V.B. Prakapenka, R. Redmer, C. Sanchez-Valle, M. Schoelmerich, S. Speziale, G. Spiekermann, B.T. Sturtevant, S. Toleikis, N. Velisavljevic, M. Wilke, C.-S. Yoo, C. Baehtz, U. Zastrau, and C. Strohm, J. Synchrotron Radiat. **28**, 688 (2021).

Supplementary Videos

Captions for supplementary videos

Supplementary video 1. This video shows the fluctuations of the x-ray beam caused by instabilities in the beamline's optics. The exposure time per frame was 20 ms. The fluctuations and the structured background overlay the signal of the object completely. Thus the flat-flied correction based on principal components as described in the main text is necessary to extract the images of the sample from the raw data.

Supplementary video 2. Integrated diffraction patterns (left) and X-ray images (right) collected during the solidification (liquid/Ga-III) of Ga (sample #1) on compression. Data were collected using the parallel beam configuration, and both imaging and diffraction data were collected with an exposure time of 50ms. **G** indicates peaks originating from the stainless steel gasket. Selected X-ray images from this video are shown in Fig. 7(a).

Supplementary video 3. Integrated diffraction patterns (left) and corresponding X-ray images (right) showing the melting (Ga-III/liquid) of Ga (sample #1) during decompression. Data were collected using the parallel beam configuration, and both imaging and diffraction data were collected with an exposure time of 25ms. **G** indicates peaks originating from the stainless steel gasket, and * indicates an unidentified peak from a contaminant phase. Selected X-ray images from this video are shown in Fig. 7(b).

Supplementary video 4. Integrated diffraction patterns (left) and corresponding X-ray images (right) showing the melting (Ga-I/liquid) of Ga (sample #3) on compression. Data were collected using the focused beam configuration, and both imaging and diffraction data were collected with an exposure time of 50ms. Selected X-ray images from this video are shown in Fig. 9(a).

Supplementary video 5. Video showing the integrated diffraction patterns (left) and corresponding X-ray images (right) collected during the crystallization (liquid/Ga-III) of Ga (sample #3) on compression. Data were collected using the focused beam configuration, and both imaging and diffraction data were collected with an exposure time of 50ms.

Supplementary video 6. Video showing the integrated diffraction patterns (left) and corresponding X-ray images (right) collected during the melting (Ga-I/liquid) of Ga (sample #4) on compression. Data were collected using the focused beam configuration, and both imaging and diffraction data were collected with an exposure time of 50ms. Selected X-ray images from this video are shown in Fig. 10(d).

Supplementary video 7. Video showing the integrated diffraction patterns (left) and corresponding X-ray images (right) collected during the crystallization (liquid/Ga-III) of Ga (sample #4) on compression. Data were collected using the focused beam configuration, and both imaging and diffraction data were collected with an exposure time of 50ms. Selected X-ray images from this video are shown in Fig. 10(e).

Supplementary video 8. Video showing the integrated diffraction patterns (left) and corresponding X-ray images (right) collected during the crystallization of Ar (sample #6) on compression. Data were collected using the focused beam configuration, and both imaging and diffraction data were collected with an exposure time of 50ms. **Cu** indicates the Cu sphere used as a pressure marker, and **G** indicates peaks originating from the stainless steel gasket. Selected X-ray images from this video are shown in Fig. 13(a).

Supplementary video 9. Video showing the integrated diffraction patterns (left) and corresponding X-ray images (right) collected during the melting of Ar (sample #6) on decompression. Data were collected using the focused beam configuration, and both imaging and diffraction data were collected with an exposure time of 50ms. **Cu** indicates the Cu sphere used as a pressure marker, and **G** indicates peaks originating from the stainless steel gasket. Selected X-ray images from this video are shown in Fig. 13(b).